Numerical study of turbulent natural convection with a descending free surface due to evaporation

Lise Ceresiat[1] and Miltiadis V. Papalexandris[1*]

[1]Institute of Mechanics, Materials and Civil Engineering, Université catholique de Louvain, 1348 Louvain-la-Neuve, Belgium.

*Corresponding author(s). E-mail(s): miltos@uclouvain.be;
Contributing authors: lise.ceresiat@uclouvain.be;

Abstract

In this paper we report on Large Eddy Simulations of natural convection in water pools with evaporation across the free surface and at the hard turbulence regime. The free surface is approximated as a free-slip top boundary. The loss of water is estimated via a dynamic and inhomogeneous evaporation model. Also, the descent of the free surface is accounted for by regularly reducing the computational domain and applying a remeshing procedure. We present results for 4 different Rayleigh numbers, ranging from $\boldsymbol{Ra = 1.35\times10^8}$ to $\boldsymbol{Ra = 10^{10}}$. Our simulations predict a slow decrease of the free-surface temperature and evaporation rate over time. This may be attributed to the descent of the free surface due to evaporation which tends to reduce the intensity of turbulent motions. On the other hand, the flow structure remains the same throughout the duration of the simulations. More specifically, the flow is organized in a large scale circulation aligned in a diagonal plane with smaller convective rolls near the corners of the domain. Also, the absence of a top hydrodynamic boundary layer enhances turbulent mixing and convective heat transfer near the free surface. This enhancement is manifested by a shift of the profile of the mean surface temperature towards the upper part of the domain, with the shift becoming more pronounced as the turbulence intensity increases. Herein we also provide results for the Nusselt number $\boldsymbol{Nu}$ and present a new $\boldsymbol{Nu - Ra}$ scaling for convection in pools and cavities that covers a large range of turbulence intensities.

Keywords: Turbulent convection; convection in pools; large eddy simulations; wall models; evaporation; non-OberbeckBoussinesq conditions; Nusselt number

1 Introduction

In this paper, we report on numerical simulations of natural convection of water with an evaporative free surface. This is a fundamental process of heat transfer in lakes and seas (Deacon, 1977; Marshall and Schott, 1999). It is also encountered in various industrial applications, such as boilers, thermal power plants, and nuclear power stations (both reactors and spent-fuel pools).

Due to its widespread occurrence in natural phenomena and practical applications, natural convection has been a topic of intense research over the years. The classical case of study is the so-called Rayleigh-Bénard Convection (RBC) which involves convection of a single fluid between two horizontal boundaries that is uniformly heated from below and cooled from above. The literature on

RBC is quite rich; see for instance (Niemala et al., 2000; Bodenschatz et al., 2000; Grossmann and Lohse, 2000, 2001; Ahlers et al., 2009; Shishkina and Thess, 2009; Lohse and Xia, 2010; Grossmann and Lohse, 2011; Chillà and Schumacher, 2012; Wang et al., 2021; Lohse and Shishkina, 2024) and references therein.

Herein we are concerned with a different configuration, namely, convection in a pool or cavity of a liquid heated from below with evaporation across its free surface. Compared to classical RBC, this configuration has been studied to a much lesser extent. Most experimental studies of it have focused on the evaporation rate and its correlation with the temperature at the free surface; see for example (Bower and Saylor, 2009b; Jodat et al., 2012; Kumar and Arakeri, 2015; Quinn Brewster, 2018; Martin and Migot, 2019; Zhang et al., 2019), as well as the review article of Poós and Varju (2019). Those and earlier studies led to the development of various models for evaporation rates such as those proposed by Quinn Brewster (2018) and Martin and Migot (2019).

An early numerical study of a similar configuration was carried out by Zikanov et al. (2002). Those authors did not consider a wall-bounded domain but, instead, prescribed periodic conditions at the horizontal directions. Later on, Hay and Papalexandris (2019) and Marichal and Papalexandris (2022) performed numerical simulations of natural convection in pools but did not account for evaporation. Those works focused on the effect of the free surface on the flow structure and convective patterns. Simulations of convection with evaporation at the free surface were presented in (Hay and Papalexandris, 2020; Hay et al., 2021). Therein, the authors studied the structure and statistical properties of the flow and also proposed correlations for the scaling between the Nusselt and Rayleigh numbers at moderate turbulence intensities. However, in those works, the descent of the free surface due to evaporation was not taken into account; accordingly the simulations were terminated while the water loss was still small (less than 3%), which limits the time-averaging period.

Recently, Liu et al. (2022) and Demou et al. (2024) presented numerical studies of convection in a box containing two immiscible fluid layers without evaporation across the free surface. (Whereas, in a different paper, Liu et al. (2022) studied convection in a box containing an oil drop surrounded by water.) In those works the, the presence of two fluids was taken into account via the introduction the volume fraction as a field variable. In the formulation of Liu et al. (2022) the volume fraction is governed by the Cahn-Hillard equation, whereas Demou et al. (2024) employed a volume-of-fluid approach.

Convection through two fluids in a box separated by an evaporative interface was studied numerically by Scapin et al. (2023) using the volume-of-fluid approach too. Those authors proposed a model for the interface temperature and validated it with 2-D numerical simulations that incorporated interface tracking. 3-D Direct Numerical Simulations (DNS) of turbulent natural convection through water/air systems in pools with evaporation and dynamic tracking of the free surface were presented by Carlier and Papalexandris (2023, 2024). DNS of the same problem and analysis of the flow structures via proper orthogonal decomposition was recently carried out by Carlier et al. (2025). However, due to the increased computational cost, those 3D simulations were limited to cases at the soft turbulence regime, *i.e.* at weak turbulent intensities.

The objective of the present work is to investigate the convection of water with an evaporative and descending free surface at the hard turbulence regime, *i.e.* at increased turbulent intensities. More specifically, we present and analyze results for 4 different Rayleigh numbers, ranging from 1.35×10^8 to 10^{10}. In our simulations, the computational domain includes only the part of the cavity containing water and does not extend above the free surface. Thus the free surface is approximated

as a horizontal free-slip boundary. Evaporation is taken into account by employing a dynamic and inhomogeneous evaporation model at the free surface, initially proposed by Martin and Migot (2019) and elaborated further by Hay et al. (2021).

For purposes of computational savings, our study does not consist of DNS, *i.e.* the grid is not sufficiently refined so as to resolve all turbulent structures. Instead, we perform Large Eddy Simulations (LES), according to which only the large turbulent scales are resolved while the small ones are suitably modeled. Moreover, we apply boundary (wall) models for the thermal and hydrodynamic boundary layers. In this manner, the grid is coarsened near boundaries and the structure of the boundary layers is modeled instead of been resolved. This approach is commonly known as Wall Modeled LES or (WMLES).

The paper is organized as follows. In section 2 we present the governing equations of the flow, and the turbulence and evaporation models employed in our simulations. In section 3 we describe the numerical setup and provide information about the computational mesh. In section 4 we present and analyze the results of our numerical simulations. First we elaborate on the flow properties of one case. Then we compare the numerical results for all of the cases considered in our study. Finally, section 5 concludes.

2 Mathematical modeling

We commence this section with the presentation of the governing equations of the flow, which are spatially filtered for the purposes of LES. Then, we describe the turbulence and boundary models and outline the dynamic evaporation model that is applied at the free surface.

2.1 Governing equations

In our study we do not invoke the Oberbeck-Boussinesq approximation. Accordingly, the flow is described by the low-Mach number approximation of the compressible Navier-Stokes-Fourier equations (Paolucci, 1982). For the purposes of LES, the low-Mach number equations are spatially filtered via the density-weighted filtering operator; this process is commonly referred to as Favre filtering. For a generic quantity ϕ, the corresponding Favre-filtered quantity $\widetilde{\phi}$ is given by $\widetilde{\phi} = \frac{\overline{\rho\phi}}{\overline{\rho}}$, where the overbar denotes a spatially filtered quantity. In dimensional form, the filtered low-Mach number equations read

$$\frac{\partial \overline{\rho}}{\partial t} + \nabla \cdot (\overline{\rho}\widetilde{\boldsymbol{u}}) = 0\,, \tag{1}$$

$$\frac{\partial (\overline{\rho}\widetilde{\boldsymbol{u}})}{\partial t} + \nabla \cdot (\overline{\rho}\widetilde{\boldsymbol{u}}\widetilde{\boldsymbol{u}}) + \nabla \overline{p} = \nabla \cdot \widetilde{\boldsymbol{\tau}} - \nabla \cdot \boldsymbol{\tau}^r + \overline{\rho}\boldsymbol{g}\,, \tag{2}$$

$$c_p \frac{\partial (\overline{\rho}\widetilde{T})}{\partial t} + c_p \nabla \cdot (\overline{\rho}\widetilde{\boldsymbol{u}}\widetilde{T}) = \frac{dp_0(t)}{dt} + \nabla \cdot \widetilde{\boldsymbol{q}} - \nabla \cdot \boldsymbol{q}^r\,. \tag{3}$$

Following standard notation, $\widetilde{\boldsymbol{u}} = (\widetilde{u}, \widetilde{v}, \widetilde{w})$ denotes the filtered velocity vector, $\overline{\rho}$ the resolved (filtered) density, p_0 the thermodynamics pressure, $\overline{p}$ the sum of the resolved dynamic and bulk-viscous pressures (Papalexandris, 2020), and c_p the specific heat capacity under constant pressure. Also $\boldsymbol{g}$ is the vector of gravitational acceleration and points downwards, to the negative y direction. Further, $\widetilde{\boldsymbol{\tau}}$ and $\widetilde{\boldsymbol{q}}$ are, respectively, the resolved viscous-stress tensor and heat-flux vector,

$$\widetilde{\boldsymbol{\tau}} = 2\mu \left(\widetilde{\boldsymbol{S}} - \frac{1}{3}(\nabla \cdot \widetilde{\boldsymbol{u}})\boldsymbol{I} \right)\,, \tag{4}$$

$$\widetilde{\boldsymbol{q}} \;=\; \lambda \nabla \widetilde{T}\,, \tag{5}$$

where μ is the shear viscosity, λ the heat conductivity, $\boldsymbol{I}$ the identity matrix, and $\widetilde{\boldsymbol{S}}$ the filtered strain-rate tensor, $\widetilde{\boldsymbol{S}} \;=\; \frac{1}{2}\left(\nabla\widetilde{\boldsymbol{u}} + (\nabla\widetilde{\boldsymbol{u}})^{\top}\right)$. Also, in (2) and (3), $\boldsymbol{\tau}^r$ and $\boldsymbol{q}^r$ are, respectively, the subgrid stress tensor and heat flux,

$$\boldsymbol{\tau}^r \;=\; \overline{\rho}\left(\widetilde{\boldsymbol{u}\boldsymbol{u}} - \widetilde{\boldsymbol{u}}\widetilde{\boldsymbol{u}}\right)\,, \tag{6}$$

$$\boldsymbol{q}^r \;=\; \overline{\rho} c_p (\widetilde{\boldsymbol{u}T} - \widetilde{\boldsymbol{u}}\widetilde{T})\,. \tag{7}$$

Both of these quantities have to be modeled.

In the problem under study, the working medium (water) has very low compressibility. Thus it is assumed to obey an isobaric equation of state, according to which the density depends on the temperature only. Since the flow domain is open, the thermodynamic pressure p_0 is constant and equal to the ambient (atmospheric) pressure. Similarly, all other fluid parameters are assumed to be functions of the temperature only.

To take into account the variations of density, specific heat capacity, viscosity and heat conductivity with temperature, we employ fourth-order polynomial fits based on tabulated data over the temperature range of interest and for $p_0 = 1$ bar from the database of Lemmon et al. (2010),

$$\overline{\phi} \;=\; c_4\widetilde{T}^4 + c_3\widetilde{T}^3 + c_2\widetilde{T}^2 + c_1\widetilde{T} + c_0\,. \tag{8}$$

The values of the coefficients of the polynomial fit for each of these quantities for the range of temperature of interest are provided in Ceresiat and Papalexandris (2025).

Herein we consider natural convection in a cubic cavity with evaporation across the top boundary, *i.e.* the free surface of the water. The bottom wall is maintained at a fixed and uniform temperature which is higher than that of the free surface. In turn, this temperature difference onsets convection of the working fluid. The initial aspect ratio of the flow domain is unity. Then the relevant dimensionless groups are the Rayleigh and Prandtl numbers,

$$Ra \;=\; \frac{|\boldsymbol{g}|\rho\beta\Delta T H^3}{\mu\alpha}\,, \qquad \text{and} \qquad Pr \;=\; \frac{\mu\, c_p}{\lambda}\,, \tag{9}$$

respectively. In the definition of the Rayleigh number, ΔT is the difference between the temperature of the bottom wall and the average temperature of the evaporative interface (free surface). Hereafter we will use the expressions *free surface* and *interface* interchangeably. In our study we take into account the descent of the free surface due to evaporation, as well as its variations. Therefore, H, ΔT and Ra vary over time.

The governing systems of equations (1)-(3) is integrated numerically via the time-accurate algorithm of Lessani and Papalexandris (2006). This algorithm combines a second-order predictor-corrector scheme for time marching with a projection (fractional-step) method for the computation of the pressure and velocity fields. The projection step amounts to taking the divergence of (2), which results in a constant-coefficient Poisson equation for the pressure. Upon discretization, this equation is reduced to a sparse linear system that is solved via an iterative linear-system solver. Spatial derivatives are discretized via second-order centered differences. The algorithm is implemented in a collocated-grid arrangement and incorporates a flux-interpolation technique (Lessani and Papalexandris, 2006, 2008) to avoid the odd-even pressure decoupling that is associated to such

grids. The algorithm has been implemented in a C/C++ code and is parallelized via the MPI protocol. It makes use of the PETSc library of data structures and linear-solvers (Balay and et al., 2025). More specifically, the Poisson equation for the pressure is solved with the PETSc routine of PFMG which is a parallel semicoarsening multigrid solver.

2.2 Subgrid and wall models

As is often the case in LES, the subgrid stress tensor $\boldsymbol{\tau}^r$ and heat flux $\boldsymbol{q}^r$ are modelled via the eddy-viscosity approach (Sagaut, 2006). This approach postulates that $\boldsymbol{\tau}^r$ represents additional viscous stresses and, therefore, its deviatoric components reads

$$\boldsymbol{\tau}^r - \frac{1}{3}\mathrm{tr}(\boldsymbol{\tau}^r)\boldsymbol{I} \;=\; -2\mu_{\mathrm{sgs}}\left(\widetilde{\boldsymbol{S}} - \frac{1}{3}(\nabla\cdot\widetilde{\boldsymbol{u}})\boldsymbol{I}\right). \tag{10}$$

Whereas, its isotropic component, $\frac{1}{3}\mathrm{tr}(\boldsymbol{\tau}^{\mathrm{r}})\boldsymbol{I}$, is absorbed by the pressure term $\overline{p}$ of equation (2). The turbulent sub-grid scale viscosity μ_{sgs} is computed via the Wall-Adapting Local Eddy-viscosity (WALE) model (Nicoud and Ducros, 1999).

Similarly, the subgrid heat flux, $\boldsymbol{q}^r$, represents additional heat flux and is modelled as

$$\boldsymbol{q}^r \;=\; -\lambda_{\mathrm{sgs}}\nabla\widetilde{T}\,. \tag{11}$$

In this equation λ_{sgs} is the turbulent heat conductivity coefficient. It is calculated by means of the Reynolds analogy: $\lambda_{\mathrm{sgs}} = \mu_{\mathrm{sgs}}c_p/Pr_{\mathrm{t}}$, with Pr_{t} being the turbulent Prandtl number. In our study we set $Pr_{\mathrm{t}} = 0.4$, as recommended by Eidson (1985) for problems of natural convection.

The use of subgrid models allows the coarsening of the computational mesh far from solid boundaries and interfaces. According to the approach of Wall Resolved LES (WRLES), the mesh is sufficiently refined close to such boundaries so as to directly resolve the boundary-layer structure. However, because of the near-boundary resolution requirements, WRLES of flows at high turbulence intensities are still too expensive from the computational point of view.

Additional coarsening of the mesh is achieved by adopting the WMLES approach whereby the boundary structures are modeled instead of been directly resolved. Similarly to subgrid modelling, models for the hydrodynamic boundary layer are based on the introduction of a turbulent viscosity relative to the boundary, μ_{t}. In our study we employ the well-known model of Cabot and Moin (2000),

$$\mu_{\mathrm{t}} \;=\; \kappa\mu y^+\left(1-\exp\left(-\frac{y^+}{A^+}\right)\right)^2, \tag{12}$$

with κ and A^+ being the von Karman and model constants, respectively. Their values are set at $\kappa = 0.41$ and $A^+ = 17$. The distance from the wall in wall units is given by $y^+ = (\rho u_\tau y)/\mu$, with u_τ being the friction velocity. The latter one is defined by $u_\tau = \sqrt{\tau_{\mathrm{w}}/\rho}$ where τ_{w} is the wall shear stress. For the computation of u_τ we employ the relation of Reichardt (1961)

$$u^+ \;=\; \frac{|u|}{u_\tau} \;=\; \frac{1}{\kappa}\ln\left(1+\kappa y^+\right) + B_1^+\left[1-\exp\left(-\frac{y^+}{B_2^+}\right) - \frac{y^+}{B_2^+}\exp\left(-\frac{y^+}{B_3^+}\right)\right]. \tag{13}$$

In this relation, the model constants are assigned the following values: $B_1^+ = 7.8$, $B_2^+ = 11$ and $B_3^+ = 3$. The velocity, density and viscosity coefficient are taken inside the boundary layer but sufficiently far from the wall (Larsson et al., 2016). The distance of this point from the wall is referred to as the *exchange location*. Equation (13) constitutes a transcendental equation for u_τ in terms of y^+ that

is solved iteratively via the Newton-Raphson method. Once u_τ is found, then one can compute the exchange location in wall units and insert the result in (12) to compute μ_t.

Similarly, thermal models are based on the concept of turbulent thermal conductivity for the boundary region, λ_t. Recently we tested different thermal boundary models in natural convection at different Ra (Ceresiat and Papalexandris, 2025). According to our comparisons, a version of the model of Kays and Crawford (1993) provided the most accurate predictions. For this reason, it has been chosen for modeling the thermal layers in the WMLES of the present study. This model makes use of the Reynolds analogy,

$$\lambda_\mathrm{t} \;=\; \mu_\mathrm{t} c_p / Pr_\mathrm{t}\,, \tag{14}$$

and introduces a correlation for the turbulent Prandtl number Pr_t in the boundary regions based on experimental data. This correlation reads,

$$Pr_\mathrm{t} \;=\; \frac{2}{Pr}\frac{\mu}{\mu_\mathrm{t}} + 0.85\,. \tag{15}$$

The experimental data that this model is derived upon are discussed in (Kays, 1994). Finally, it is worth adding that since the free surface is modeled as a free-slip top boundary, a thermal boundary layer is developed therein but not a hydrodynamic one. This implies that near the free surface we employ λ_t and μ_sgs instead of μ_t.

2.3 Evaporation model

The evaporation of water across the free surface is accounted for by solving a dynamic evaporation model. This model was proposed by Martin and Migot (2019) and is inhomogeneous in the sense that it is applied locally at each segment of the free surface. Its outcome is used to calculate the normal derivative of the temperature which, in turn, is assigned as a boundary condition at the free surface. This process is performed at every time step depends only on the temperature in the corresponding boundary cell and on fixed ambient conditions. Below we provide an outline of the evaporation model; for full details the reader is referred to (Hay et al., 2021).

The energy balance at the free surface reads

$$\lambda_\mathrm{int}\frac{\partial \widetilde{T}}{\partial y} \;=\; \left(\dot{q}''_\mathrm{conv} + \dot{q}''_\mathrm{evap}\right)\,. \tag{16}$$

The left-hand side describes heat conduction at the free surface. Therein λ_int is the thermal conductivity of the water at the free surface and is computed from (8) using the free-surface temperature from the previous time step. Also $\dot{q}''_\mathrm{conv}$ is the heat loss due to convection at the gas side (outside the computational domain), and $\dot{q}''_\mathrm{evap}$ is the heat loss due to evaporation. This equation serves as a non-zero Neumann condition for the temperature on top and requires estimates for $\dot{q}''_\mathrm{conv}$ and $\dot{q}''_\mathrm{evap}$.

At the gas side, transition from the interface conditions to the ambient ones is assumed to occur over a layer referred to as *film*. The ambient conditions are assumed to be fixed and known. The conditions at the free surface are taken to be those from the previous time step.

The vapor partial pressure at the free surface and at ambient conditions is computed from the corresponding temperature via the Wagner equation (Poling et al., 2001). This allows to evaluate the free-surface and ambient vapor concentration, $Y_\mathrm{v,int}$ and $Y_\mathrm{v,\infty}$ respectively, and the density of the gas/vapor mixture.

We then consider the average properties of the air/vapor mixture in the film, denoted with the subscript "f": film temperature T_f, film density ρ_f and so on and so forth. These are taken to be the averages between the respective free-surface and ambient properties. Also, the film conductivity κ_f and viscosity ν_f are computed from the kinetic theory of gases for a two-component mixture (Hay et al., 2021).

The term $\dot{q}''_\mathrm{conv}$ is computed via Newton's law of convection. In other words, the convective heat loss is proportional to the difference between the resolved free-surface temperature, $\widetilde{T}_\mathrm{int}$, and the ambient temperature, T_∞,

$$\dot{q}''_\mathrm{conv} \;=\; h\left(\widetilde{T}_\mathrm{int} - T_\infty\right) . \tag{17}$$

The heat-transfer coefficient h is estimated from the following correlation for a horizontal flat surface of width H_0 that is warmer than the ambient air above (Lloyd and Moran, 1974),

$$\frac{h\ H_0}{\lambda_\mathrm{f}} \;=\; 0.54 {Ra_\mathrm{t}}^{0.25} . \tag{18}$$

In this relation, λ_f is the film conductivity, *i.e.* the conductivity of the air/vapor mixture in the film. Also, Ra_t is the gas-side thermal Rayleigh number, $Ra_\mathrm{t} = \frac{|\boldsymbol{g}|\beta_\mathrm{f}(\widetilde{T}_\mathrm{int}-T_\infty)H_0^3}{\kappa_\mathrm{f}\nu_\mathrm{f}}$, with β_f, being the thermal expansion coefficient of air in the film.

The heat loss due to evaporation reads,

$$\dot{q}''_\mathrm{evap} \;=\; \dot{m}'' h_\mathrm{lv} , \tag{19}$$

where $\dot{m}''$ is the evaporative mass flux and h_lv the enthalpy of evaporation. The latter one is computed from a Watson relation (Viswanath and Kuloor, 1967),

$$h_\mathrm{lv} \;=\; 2256.4 \left(\frac{T_\mathrm{c} - \widetilde{T}_\mathrm{int}}{T_\mathrm{c} - T_\mathrm{b}}\right)^n . \tag{20}$$

with the exponent $n = 0.283$. In this equation T_c is the critical temperature of air and T_b is the boiling temperature of water at ambient pressure. Also, the evaporative mass flux is estimated from the relation (Lienhard and Lienhard, 2019),

$$\dot{m}'' \;=\; Sh \frac{\rho_\mathrm{f} D_\mathrm{f}}{H_0} \ln\left(1 + B_\mathrm{m}\right) . \tag{21}$$

In this equation, D_f is the film air-vapor diffusivity, Sh the Sherwood number and B_m the mass-transfer driving force. For the diffusivity, expressed in SI units, we employ the correlation (Marrero and Mason, 1972),

$$D_\mathrm{f} \;=\; 1.87 \times 10^{-10} \frac{T_\mathrm{f}^{2.072}}{p_0} . \tag{22}$$

Also, with respect to (21), the expression for B_m reads,

$$B_\mathrm{m} \;=\; \frac{Y_{\mathrm{v},\infty} - Y_{\mathrm{v,int}}}{Y_{\mathrm{v,int}} - 1} , \tag{23}$$

and the Sherwood number is estimated from the following correlation (Bower and Saylor, 2009a),

$$Sh \;=\; 0.23\ {Sc}^{0.333} {Ra_\mathrm{c}}^{0.321} , \tag{24}$$

where $Sc = \frac{\nu_\mathrm{f}}{D_\mathrm{f}}$ is the film Schmidt number and $Ra_\mathrm{c} = \frac{|\boldsymbol{g}|(\rho_\infty - \rho_\mathrm{int})H_0^3}{D_\mathrm{f}\mu_\mathrm{f}}$ the concentration Rayleigh number of the film. We recall that H_0 is also the width of the water column since the initial aspect ratio is unity.

Finally, the instantaneous height of the free surface, $H(t)$, is given in terms of the cumulative mass loss due to evaporation and reads,

$$H(t) \;=\; H_0 - \int_0^t \left\langle \frac{\dot{m}''}{\overline{\rho}_\mathrm{int}} \right\rangle_{xz} dt\,, \tag{25}$$

where $\overline{\rho}_\mathrm{int}$ is the resolved water density at the free surface.

3 Numerical setup

In this section, we elaborate on the numerical setup of our study and the remeshing procedure that accounts for the descent of the free surface. In the following, the hat symbol $\hat{}$ is used to denote a dimensionless quantity. Also the area average of a generic quantity ϕ in the horizontal x and z directions is denoted by the $\langle\phi\rangle_{xz}$. Whereas the combined time and area average of ϕ is denoted by brackets without subscript, $\langle\phi\rangle$. Further, ϕ' stands for the fluctuation of ϕ, *i.e.* $\phi' = \phi - \langle\phi\rangle$.

We consider natural convection of liquid water in a pool whose width (dimensions in the horizontal directions) is equal to H_0. The initial height of the pool (dimension in the vertical y direction) is also H_0. Due to evaporation, the height of the water column drops over time. Accordingly, the height of the computational domain drops as well. The free surface is approximated as a flat, horizontal, free-slip boundary. In view of the physical parameters in the cases considered herein, this approximation is valid on the basis of the findings of Liu et al. (2021) for two-layer thermal convection. The instantaneous height of the free surface is denoted by H; see Figure 1 below.

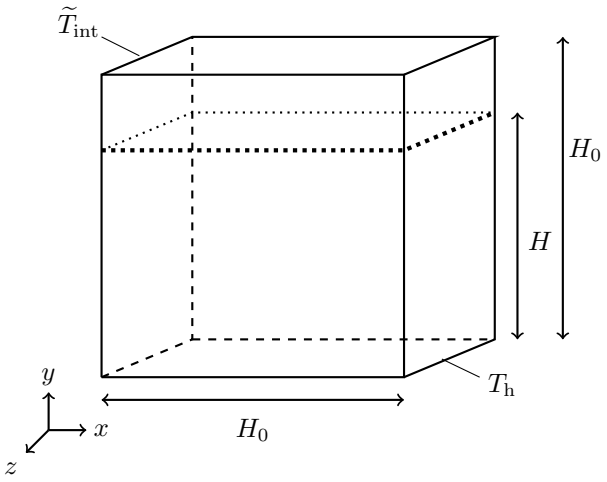


Fig. 1 Schematic representation of the flow domain: the initial height of the free surface (top boundary) is H_0 and the instantaneous one is H

Initially the fluid is at rest. The temperature of the bottom wall, T_h, is fixed. The initial temperature at the free surface $T_{\mathrm{int},0}$ is uniform and lower than T_h. In other words, the fluid is unstably stratified and subject to natural convection. On the other hand, the temperature at the free surface varies both in time and in the horizontal directions.

For non-dimensionalization purposes, the reference length is the initial height of the domain H_0. The reference velocity is the initial free-fall velocity, $u_{\rm ff} = \sqrt{|\boldsymbol{g}| H_0 \beta_{\rm ref} \Delta T_0}$, with ΔT_0 being the initial top-bottom temperature difference: $\Delta T_0 = T_{\rm h} - T_{{\rm int},0}$. The free-fall time $t_{\rm ff} = H_0/u_{\rm ff}$ serves as the reference time scale. Whereas the reference temperature is the average between the bottom temperature and the initial temperature on top, $T_{\rm ref} = (T_{\rm h} + T_{{\rm int},0})/2$. The reference pressure $p_{\rm ref}$ is the ambient pressure above the free surface. Also, reference values of the fluid parameters are those at the reference temperature and pressure.

The Rayleigh number based on ΔT_0 and H_0 is referred to herein as the initial Rayleigh number and denoted by Ra_0. In the present study we have performed simulations of 4 cases at different Ra_0. The initial domain height, free-fall velocity and free-fall time for each case are provided in Table 1 below.

The grid spacing in the bulk is determined via estimates of the Taylor microscale of turbulent motions and the Batchelor scale of thermal fluctuations. The estimate of the Taylor microscale reads (Peng et al., 2006),

$$\hat{\eta}_l \;=\; \frac{\sqrt{15}\,\hat{u}^*}{\sqrt{Ra_0\,(Nu_0 - 1)}}\,, \tag{26}$$

where $\hat{u}^*$ is representative of the dimensionless velocity in the bulk,

$$\hat{u}^* \;=\; \sqrt{0.068\,{Ra_0}^{0.91} + 0.012\,{Ra_0}^{0.96}}\,, \tag{27}$$

and Nu_0 is the initial value of the (global) Nusselt number. The Batchelor scale for a fluid with Prandtl number $Pr > 1$ is estimated from the relation (Stevens et al., 2010),

$$\hat{\eta}_\theta \;=\; \left(\frac{1}{Ra_0\,Pr\,Nu_0}\right)^{1/4}\,. \tag{28}$$

For our simulations we have followed the procedure of Hay et al. (2021) according to which the maximum length of a computational cell in the bulk is chosen to be the smaller between one half of the Taylor microscale, $\hat{\eta}_l/2$, and the relaxed thermal microscale, $4\pi\hat{\eta}_\theta$. With regard to Nu_0, it is estimated from the following correlation for natural convection in a cavity (Hay and Papalexandris, 2020),

$$Nu \;=\; 0.178\,{Ra_0}^{0.301}\,. \tag{29}$$

As mentioned above, in the context of boundary-layer modeling for WMLES, the turbulent viscosity and conductivity are evaluated at the so-called exchange location. This location is determined on the basis of estimates of the thicknesses of the hydrodynamic and thermal boundary layers, $\hat{\delta}_u^{\rm es}$ and $\hat{\delta}_\theta^{\rm es}$ respectively. Herein we employ the estimates derived by Shishkina et al. (2010) on the basis of the Prandtl-Blasius theory. For fluids with $1 < Pr \leq 3$ these estimates read,

$$\hat{\delta}_u^{\rm es} \;=\; \frac{1}{2Nu}\,Pr^{(0.357 - 0.022\ln Pr)}\,, \tag{30}$$

$$\hat{\delta}_\theta^{\rm es} \;=\; \frac{1}{2Nu}\,. \tag{31}$$

The dimensionless exchange location $\hat{h}_{\rm wm}$ should lie inside the hydrodynamic boundary layer. As a general guideline (Kawai and Larsson, 2012; Larsson et al., 2016), it is recommended to set it equal to 20% of the layer thickness, *i.*e. $\hat{h}_{\rm wm} = 0.2\hat{\delta}_u^{\rm es}$. This guideline has also been followed in the present

study. Further, the exchange location for the thermal model is the center of the second layer of cells off the boundary. Numerical experiments that we conducted in the context of an earlier study (Ceresiat and Papalexandris, 2025) have shown that this choice works well in practice.

Finally, the computational mesh is stretched (coarsened) from a wall towards the center of the domain via a hyperbolic tangent function. In our simulations, the number of computational cells is the same in all directions. Details for the computational mesh employed for each case considered herein are also provided in Table 1.

Table 1 Reference values and mesh properties for the cases considered in our study. N is the number of grid cells in each direction, $\Delta\hat{x}_{\min}$ is the minimum grid spacing (near the boundaries), and $\Delta\hat{x}_{\max}$ is the maximum grid spacing (at the center of the domain). The estimated thicknesses of the boundary layers are from equations (30) and (31)

	Ra_0	H_0 [m]	u_{ff} [m/s]	t_{ff} [s]	N	$\Delta\hat{x}_{\min}$	$\Delta\hat{x}_{\max}$	$\hat{\delta}_u^{es}$	$\hat{\delta}_\theta^{es}$
case 1	1.35×10^8	0.045	0.0613	0.73	48	6.41×10^{-3}	3.56×10^{-2}	1.28×10^{-2}	10^{-2}
case 2	10^9	0.088	0.0854	1.03	88	3.48×10^{-3}	1.91×10^{-2}	7×10^{-3}	5.5×10^{-3}
case 3	5×10^9	0.150	0.1115	1.35	130	2.4×10^{-3}	1.27×10^{-2}	4.3×10^{-3}	3.4×10^{-3}
case 4	10^{10}	0.189	0.1251	1.51	190	1.42×10^{-3}	9.14×10^{-3}	3.51×10^{-3}	2.74×10^{-3}

The descent of the free surface is accounted for via remeshing in the y direction while keeping the number of cells constant. With the aim of keeping the computational cost at reasonable levels, the remeshing procedure is not applied at every time step but only once the height of the free surface H has been decreased by a certain amount. In order to fix ideas, let t^n represent the time after n time steps. The solution at t^n is assumed known. Also, let Δt^n the current time step, *i.e.* $\Delta t^n = t^{n+1} - t^n$. Now let H^* denote the height of the computational domain at t^n and up until the next remeshing. Since remeshing is not applied at every time step, H^* is slightly larger than the instantaneous height of the free surface H^n. In the next time step t^{n+1}, the new free-surface height H^{n+1} is computed via discretization of (25),

$$H^{n+1} \;=\; H^n - \Delta t^n \;\left\langle \frac{\dot{m}''}{\overline{\rho}_{\text{int}}} \right\rangle_{xz}^{n} . \tag{32}$$

When the normalized height difference $\frac{H^* - H^{n+1}}{H^*}$ exceeds a certain threshold, then the sizes of all cells in the y direction are reduced by the same factor $R = \frac{H^{n+1}}{H^*}$ so that the new height of the computational domain become equal to H^{n+1}. In the context of our study we examined different values of the aforementioned threshold and it was determined that the value 0.005 provides a good balance between accuracy of results and computational cost. Schematically, the remeshing procedure is described as follows,

$$\text{if} \quad \frac{H^* - H^{n+1}}{H^*} \;>\; 0.005\,, \qquad \text{then} \quad \begin{cases} R = \frac{H^{n+1}}{H^*}\,. \\ H^* = H^{n+1}\,. \end{cases} \tag{33}$$

Once the height of the computational domain is modified, then the cell-averaged values of the flow variables are assigned to the new cell centers. Since the difference between the previous and the new heights of the cell centers is very small (equal to the threshold value), the computational error induced by the reassignment of the flow variables is also very small. The evolution of the grid is illustrated in Figure 2 which shows the initial and final grid resolution for the simulation of case 1.

It is noted that this remeshing procedure keeps the number of cells constant but increases their aspect ratio. Accordingly there are certain limits to its applicability. More specifically, this procedure

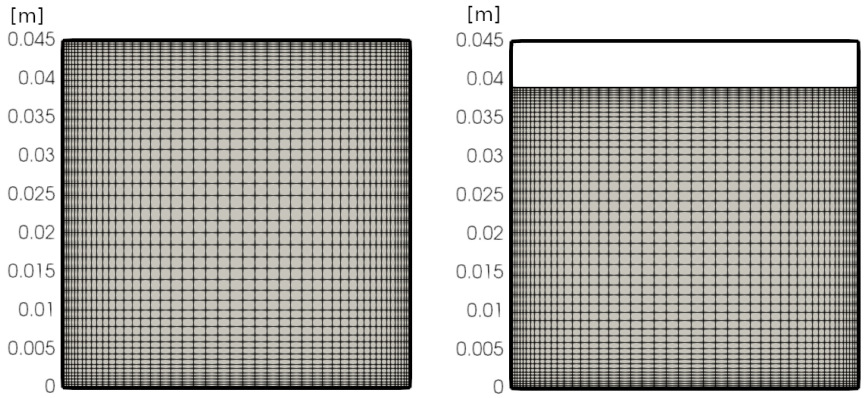


Fig. 2 Initial and final grid resolution at the x and y directions for the simulation of case 1. Left: initial mesh. Right: final mesh at $t = 2000\, t_{\mathrm{ff}}$

is valid only up to the point where the cell aspect ratio does not get too large. In the simulations presented herein the total height loss is approximately 10%. For such values of height loss, this remeshing procedure did not result in any sort of numerical instability.

With regard to boundary conditions, as mentioned above, the bottom wall is kept at fixed temperature T_{h}. While the sidewalls are assumed to be adiabatically isolated and, therefore, a zero-Neumann thermal condition is assigned to them. A non-zero Neumann condition is prescribed for the temperature at the free surface, computed via the evaporation model that was outlined above. Also, zero-slip kinematic conditions are assigned at the walls and a free-slip one at the free surface.

Finally, with regard to initial conditions, the fluid is assumed to be initially at rest and is assigned a linear temperature profile between T_{h} and $T_{\mathrm{int},0}$.

4 Numerical Results

In this section, we present the results of the simulations of the 4 cases mentioned above; namely $Ra_0 = 1.35{\times}10^8$, 10^9, $5{\times}10^9$ and 10^{10}. Both the bottom and initial free-surface temperatures are the same in all cases, $T_{\mathrm{h}} = 366$ K and $T_{\mathrm{int},0} = 352.6$ K. Accordingly, the reference temperature is the same too, $T_{\mathrm{ref}} = 359.3$ K. Also, the ambient temperature is set equal to $p_{\mathrm{ref}} = 1$ bar. The physical parameters of liquid water at the reference condition are given in Table 2.

Table 2 Physical parameters of liquid water at the reference conditions $T_{\mathrm{ref}} = 359.3$ K and $p_{\mathrm{ref}} = 1$ bar

Pr	ρ_{ref} [kg/m^3]	$c_{p,\mathrm{ref}}$ [J/(kg K)]	β_{ref} [1/K]	μ_{ref} [kg/(m s)]	λ_{ref} [W/(m K)]	α_{ref} [m^2/s]
2.06	967.86	4201.2	$6.7{\times}10^{-4}$	$3.29{\times}10^{-4}$	0.67	$1.64{\times}10^{-7}$

In each simulation, we start computing time averages at $t = 300\ t_{\mathrm{ff}}$. For the range of Rayleigh numbers considered herein, this time is deemed sufficient for the flow turbulence to reach stationary state and all transient effects to be washed out (Stevens et al., 2010). The final times of the simulations are as follows: 2000 t_{ff} for cases 1 and 2, 1500 t_{ff} for case 3 and 1000 t_{ff} for case 4. The simulation time is reduced in cases 3 and 4 for purposes of computational savings. Nonetheless, the

selected final times in cases 3 and 4 are still sufficient to allow for substantial water loss and descent of the free surface.

It is noted that, since the water height drops due to evaporation, technically the flow does not reach stationary state. However, under the conditions considered herein, the characteristic time scale of evaporation is much larger than the characteristic time scales of the flow turbulence; a comparison of the relevant timescales for case 2 is provided in the following subsection. Due to the large disparity between the evaporation and hydrodynamic time-scales, it is still meaningful to perform time averaging of the numerical results, while keeping in mind that time-averaged quantities will eventually evolve over very long periods of time.

Below we first analyze the flow structure and statistical properties of case 2, which plays the role of the nominal case. Subsequently, we present a comparison of the properties of the 4 cases. Emphasis is placed on the descent and temperature of the free surface and on the Nu–Ra scaling.

4.1 Results and discussion for case 2 ($Ra_0 = 10^9$)

According to our simulations, the flow is organized in a single-roll Large-Scale Circulation (LSC). Further, the absence of a hydrodynamic boundary layer on top allows for stronger turbulent motions and mixing in the upper part of the domain, thereby enhancing convection. These observations can readily be inferred from Figure 3 which shows plots of the instantaneous streamlines colored with the temperature field at two different time instances. These instances correspond to the start of time averaging, $t = 300\ t_{\mathrm{ff}}$, and to the end of the simulation, $t = 2000\ t_{\mathrm{ff}}$.

More specifically, in these plots, we observe significant spatial variations (horizontal gradients) of the temperature at the free surface. These gradients result in a spotty temperature distribution, *i.e.* in patches of higher or lower temperature. In fact, at $t = 2000\ t_{\mathrm{ff}}$ there are slightly more cold patches (shown in blue color) than at $t = 300\ t_{\mathrm{ff}}$. This is an indication that the average free-surface temperature has decreased over time.

Further, in both time instances (300 and 2000 $\mathrm{t_{ff}}$), we notice a concentration of warm patches near the left corner of the free surface. This corresponds to the impingement of the LSC at the free surface. In other words, the LSC is aligned in the diagonal plane that extends from the left to the right edges of the domain shown in Figure 3. The fact that the impingement point is visible over a prolonged time period indicates that the LSC is a persistent convective structure and its stability is not affected by the descent of the free surface or the temperature variations therein.

In Figure 4 we provide color plots of the instantaneous temperature at the diagonal plane of alignment of the LSC, superimposed with in-plane velocity vector plots, at 300 and 2000 t_{ff}. These plots clearly depict the LSC, with ascending warm water at the left edge and descending colder water at the right edge. We can also observe the formation of secondary convective rolls at the four corners of the diagonal plane.

Next we examine the profile of the area-averaged temperature of the interface in dimensionless form, $\frac{\langle \widetilde{T}_{\mathrm{int}} \rangle_{xz}}{T_{\mathrm{ref}}}$. Its evolution is plotted in Figure 5. Overall, the free-surface temperature does not remain constant but decreases slightly over time. This may be attributed to the decrease of the water height due to evaporation, which results in a considerable drop of the Rayleigh number. For example, at $t = 2000\, t_{\mathrm{ff}}$, the Rayleigh number is approximately 75% of Ra_0. The drop of Ra means that the intensity of the turbulent motions attenuates over time. Accordingly, as time advances,

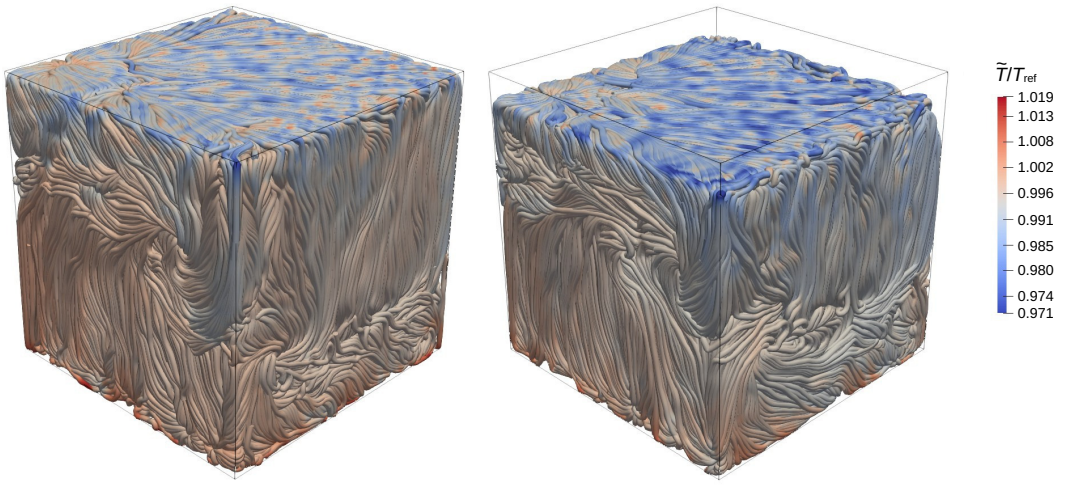


Fig. 3 Case 2: instantaneous streamlines colored by the temperature at $t = 300\,t_{\text{ff}}$ (left) and $t = 2000\,t_{\text{ff}}$ (right). The concentration of warm patches near the left corner of the free surface marks the impingement point of the LSC

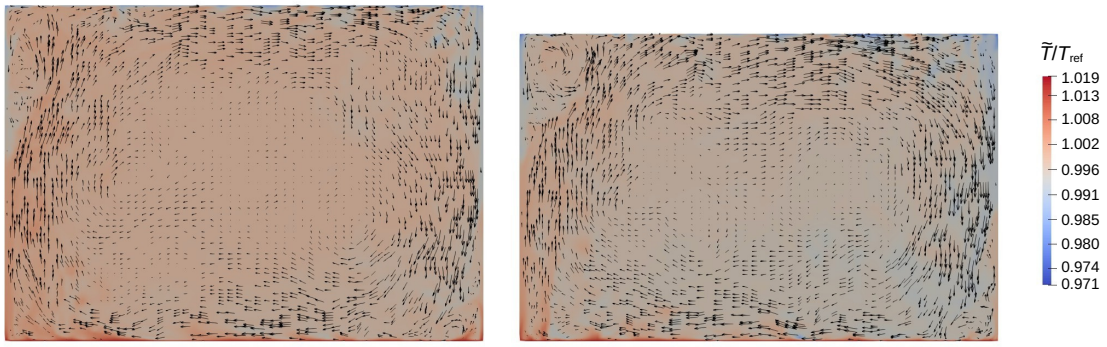


Fig. 4 Case 2: color plots of the temperature at the diagonal plane of alignment of the LSC, superimposed with in-plane velocity vector plot, at $t = 300\,t_{\text{ff}}$ (left) and $t = 2000\,t_{\text{ff}}$ (right)

diffusive heat transfer is favored over convective one, which in turn causes a slow decrease of $\langle \widetilde{T}_{\text{int}} \rangle_{xz}$. In other words, Ra drops over time and so does Nu.

Further, the profile of $\langle \widetilde{T}_{\text{int}} \rangle_{xz}$ is not monotonic but exhibits low-amplitude oscillations. Similar profiles were reported by Carlier and Papalexandris (2024) who performed DNS of convection in water/air systems; those simulations involved dynamic interface tracking but considered cases at the soft turbulence regime. Since such low-amplitude oscillations of $\langle \widetilde{T}_{\text{int}} \rangle_{xz}$ have been predicted by different numerical methodologies and at different Rayleigh numbers, we may deduce that they do not constitute a numerical artifact but represent actual thermal oscillations at the free surface due to turbulence.

The evolution of the evaporative mass flux and descent of the free surface are plotted in Figures 6a and 6b respectively. It can be readily inferred that the evolution of $\langle \dot{m}'' \rangle_{xz}$ is practically identical to that of the average free-surface temperature $\langle \widetilde{T}_{\text{int}} \rangle_{xz}$. This is not surprising since, according to the evaporation model employed herein and for fixed ambient conditions above the free surface, $\langle \dot{m}'' \rangle_{xz}$ is controlled by $\langle \widetilde{T}_{\text{int}} \rangle_{xz}$. More specifically, $\langle \dot{m}'' \rangle_{xz}$ depends monotonically on $\langle \widetilde{T}_{\text{int}} \rangle_{xz}$. Accordingly,

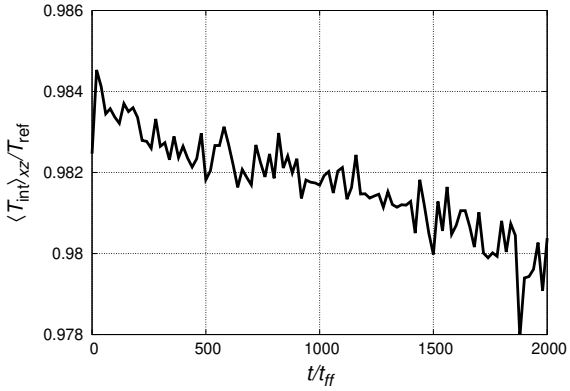


Fig. 5 Case 2: evolution of the mean (area-averaged) temperature of the free surface

$\langle \dot{m}'' \rangle_{xz}$ does not remain constant but decreases slightly. Further, its profile exhibits the same low-amplitude oscillations as that of $\langle \widetilde{T}_{\rm int} \rangle_{xz}$.

It is interesting to note that, in this particular case and for $T_{\rm ref}$ =359.3 K, the average free-surface temperature takes values between 353.1 and 352.6 K. While, as shown in Figure 6a, the evaporative mass flux takes values between 3.4 and 3.9 g/(m^2 s). These predictions are very close to the experimental data of Martin and Migot (2019) and easily within the experimental error provided therein.

Also, according to our simulations, the descent of the free surface is practically steady, as shown in Figure 6b. This implies that the time variations of the evaporative flux and free-surface density are too small to impact significantly the evolution of the water height.

It is worth adding that the characteristic time-scale of evaporation is given by $t_{\rm lv} = \frac{\rho_{\rm ref} H_0}{\langle \dot{m}'' \rangle_{xz}}$. Whereas the largest hydrodynamic time-scale is given by $t_{\rm ff} = \frac{H_0}{u_{\rm ff}}$. For case 2, and for $\langle \dot{m}'' \rangle_{xz} =$ 3.8 g/(m^{2}s), $t_{\rm lv}$ is at the order of 2.24×10^4 s. On the other hand, according to table 1, $t_{\rm ff} \approx 1.03$ s. In other words, $t_{\rm lv}$ is 4 orders of magnitude larger than $t_{\rm ff}$, which confirms our assumption that the time-scale of evaporation is much larger than the hydrodynamic time-scales.

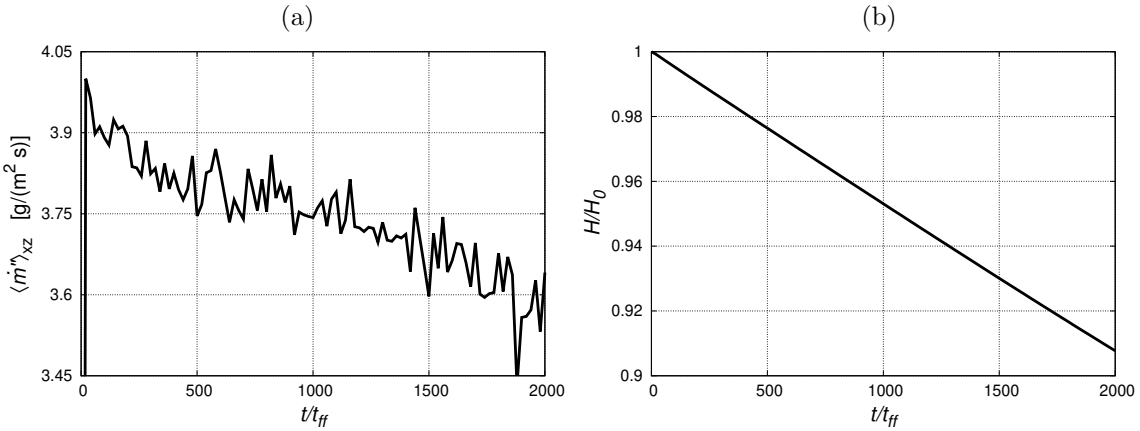


Fig. 6 Case 2: (a) evolution of the evaporative mass flux $\langle \dot{m}'' \rangle_{xz}$; (b) evolution of the water height H

Next we examine the profile of the normalized temperature $\Theta(t)$, defined as,

$$\Theta(t) \;=\; \frac{\langle \widetilde{T} \rangle_{xz} - \frac{T_{\rm h} + \langle \widetilde{T}_{\rm int} \rangle_{xz}}{2}}{T_{\rm h} - \langle \widetilde{T}_{\rm int} \rangle_{xz}} \,. \tag{34}$$

Profiles of the mean (time and area-averaged) normalized temperature $\langle \Theta \rangle$ for three different time-averaging periods, *i.e.* for three different final heights are provided in Figure 7. The averaging periods start at $t = 300\, t_{\rm ff}$ and terminate at $t = 1000$, 1500 and 2000 $t_{\rm ff}$, respectively. With regard to the computation of these profiles, it is noted that since the water height $H(t)$ drops in the course of the simulation, then we first compute the instantaneous profile of $\Theta(t)$ as a function of y scaled by the instantaneous values of $H(t)$ and then we take time averages.

According to this figure, the profile of $\langle \Theta \rangle$ varies only marginally as the time-averaging period increases. Further, it has the same characteristics as those predicted in earlier simulations at lower *Ra* (Hay and Papalexandris, 2019, 2020). More specifically, the profile is not symmetric about the midheight plane but is shifted to the left, *i.e.* towards the upper part of the pool. This is due to the free-slip condition on top which excludes the formation of a hydrodynamic boundary layer, thereby enhancing convective motions. Another feature of this asymmetry is that the thermal boundary layer at the free surface is slightly thinner than at the bottom well. Nonetheless, $\langle \Theta \rangle$ varies slightly in the bulk and its gradients are essentially confined in the boundary layer regions. This is an indication of efficient thermal mixing due to turbulent convection. It is worth adding that the profile of $\langle \Theta \rangle$ is very close to the one predicted in the simulations of (Ceresiat and Papalexandris, 2025) which did not account for evaporation and free-surface descent.

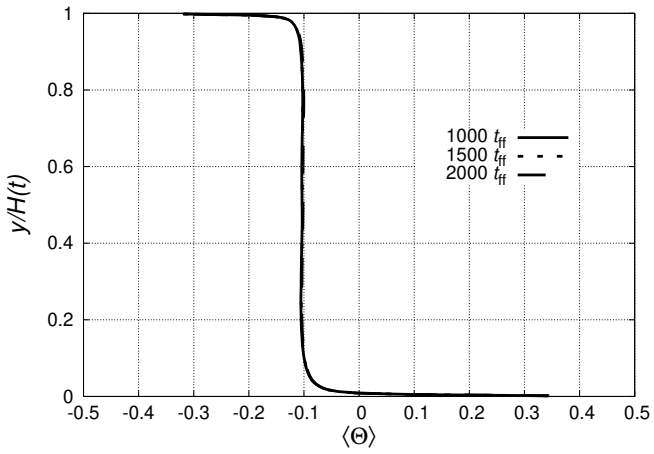


Fig. 7 Case 2: profiles of the mean normalized temperature $\langle \Theta \rangle$ for different time-averaging periods.

With regard to flow statistics, the rms profiles of the fluctuations of the velocity components along the vertical (y) direction are shown in Figure 8 for the three time-averaging periods mentioned above. More specifically, in Figure 8a we provide the plot of the rms of the fluctuations of the vertical velocity, $v_{\rm rms}$, and in Figure 8b the plot of the rms of the fluctuations of the in-plane velocity, $\bar{u}_{\rm rms} = \sqrt{\langle u'^2 + w'^2 \rangle}$. Again, these profiles exhibit the same trends as those predicted by WRLES of convection at lower *Ra* that did not account for the descent of the free surface (Hay and Papalexandris, 2020; Hay et al., 2021).

More specifically, $v_{\rm rms}$ assumes an almost parabolic profile with its peak close to midheight. Whereas $\bar{u}_{\rm rms}$ has a peak at the edge of the bottom boundary layer, a global maximum at the free surface, and falls off away from the horizontal boundaries. In the bulk, $\bar{u}_{\rm rms}$ varies only slightly; but it still exhibits two minima and a local peak in between them and near the midheight. Further, in Figure 8 we can observe some small differences between the rms profiles computed over different time-averaging periods. For example, the peak of $v_{\rm rms}$ falls slightly as the averaging period increases and so do the two minima of $\bar{u}_{\rm rms}$. This is attributed primarily to the decrease of turbulence intensity in the course of the simulation due to the drop of the water height, which is manifested by the decrease of Rayleigh number. We also note that as the water height drops, the aspect (width-to-height) ratio rises, which also affects the properties of turbulent convection. However, the total height in the simulation is approximately 9%. This means that the aspect ratio has varied by 9% only, whereas the Rayleigh number has been decreased by approximately 25%. In other words, the increase of the aspect ratio remains mild and is not expected to influence significantly the flow properties.

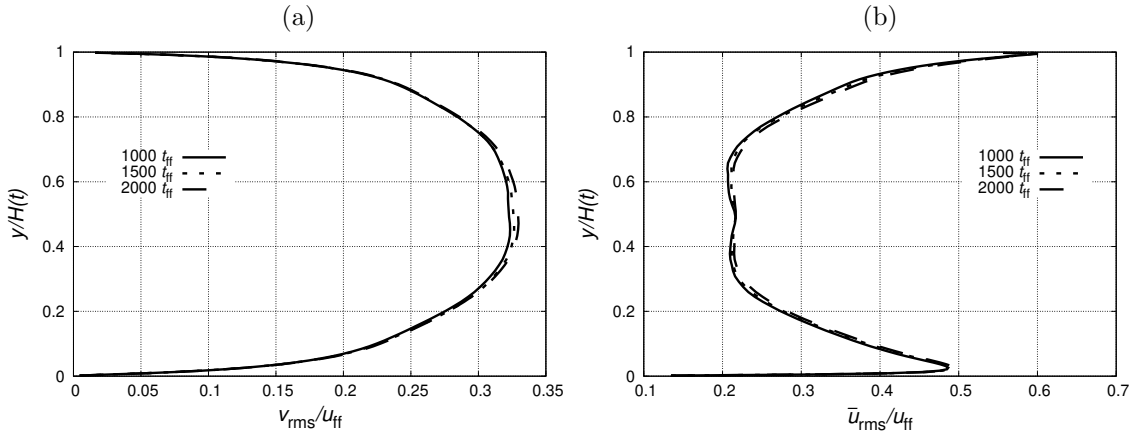


Fig. 8 Case 2: rms profiles of the velocity fluctuations for different time-averaging periods. (a) vertical velocity $v_{\rm rms}$; (b) in-plane velocity, $\bar{u}_{\rm rms} = \sqrt{u'u' + w'w'}$

We proceed to examine the predictions for the (local) Nusselt number along the y direction, $Nu(y)$. In the context of LES, $Nu(y)$ is the sum of three components: the convective, diffusive and turbulent (subgrid) ones,

$$Nu(y) \;=\; \underbrace{\sqrt{RaPr}\,\langle\hat{\rho}\hat{v}\Theta\rangle}_{Nu_{\rm conv}} - \underbrace{\langle\hat{\lambda}\frac{\partial\Theta}{\partial\hat{y}}\rangle}_{Nu_{\rm diff}} - \underbrace{\langle\hat{\lambda}_t\frac{\partial\Theta}{\partial\hat{y}}\rangle}_{Nu_{\rm turb}}\,. \tag{35}$$

The diffusive component involves the dimensionless conductivity $\hat{\lambda}$ which is computed from the resolved temperature $\widetilde{T}$, while the turbulent one involves the dimensionless turbulent conductivity $\hat{\lambda}_t$. In Figure 9a and 9b we have plotted the profiles of $Nu_{\rm conv}$ and $(Nu_{\rm diff} + Nu_{\rm turb})$, respectively, and for the three time-averaging periods mentioned above, *i.e.* up to $t = 1000$, 1500 and 2000 $t_{\rm ff}$. When the flow turbulence reaches a stationary state, $Nu(y)$ should be constant and equal to the global Nusselt number Nu. Further, in the bulk, the sum of the diffusive and turbulent components should vanish, *i.e.* the convective component should equal to $Nu(y)$ in the bulk. The profiles shown in Figure 9 confirm these characteristics. Nonetheless, the profiles of $Nu_{\rm conv}$ and $(Nu_{\rm diff} + Nu_{\rm turb})$ are not exactly constant but exhibit some mild variations in the bulk. Most likely, these variations

represent numerical artifacts due to the coarseness of the mesh, which is a known shortcoming of WMLES (Ceresiat and Papalexandris, 2025).

Besides that, it is interesting to observe that the value of the global Nusselt number, which is equal to $Nu_{\rm conv}$ in the bulk, decreases mildly as the period of time-averaging increases. Evidently, this is due to the ongoing evaporation which results in loss of water height and drop of the Rayleigh number in the course of the simulation.

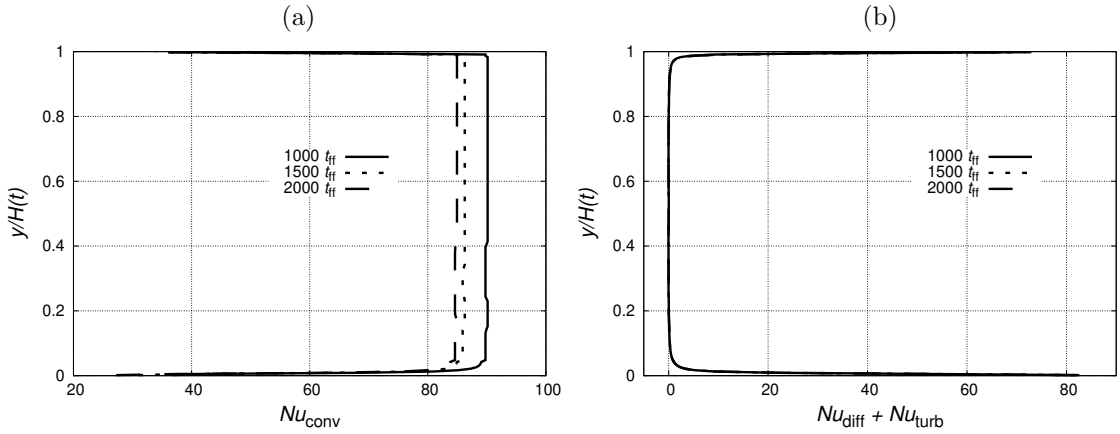


Fig. 9 Case 2: profiles of the components of the Nusselt number for three different time-averaging periods. (a) Convective part; (b) diffusive plus turbulent parts

Further in Table 3 we compare the numerical predictions of Nu with those from correlation (29), during the aforementioned time-averaging periods. In the same table we also provide the values of the instantaneous Rayleigh number Ra, free-surface height H and bottom-top temperature difference $\Delta\widetilde{T} = T_{\rm h} - \langle\widetilde{T}_{\rm int}\rangle_{xz}$ at the end of each time-averaging. At $t = 1000\,t_{\rm ff}$ the deviation between the predictions of our WMLES and the correlation (29) is approximately 4%, but it reduces to 1% at later times. Nonetheless, it should be noted that the correlation (29) has been derived from numerical simulations with Ra between 7.5×10^6 and 1.3×10^8 and, therefore, it is not necessarily accurate in the range of Ra examined herein.

Table 3 Case 2: predictions of the Nusselt number from our WMLES and from correlation (29) at 3 different times. In the same table, we provide the instantaneous values of H, $\Delta\widetilde{T}$ and Ra. For this case, $H_0 = 0.088$ m and $Ra_0 = 10^9$

$t/t_{\rm ff}$	H [m]	$\Delta\widetilde{T}$ [K]	Ra	Nu	Corr. (29)
1000	0.0839	12.88	8.91×10^8	91.47	87.98
1500	0.0819	13.5	8.68×10^8	87.64	87.28
2000	0.0799	13.35	7.98×10^8	86.35	85.10

In summary, our simulations predict a slow decrease of the free-surface temperature and the evaporation rate. Nonetheless, the rate of descent of the water level remains practically steady. Even though the Rayleigh number drops over time due to water evaporation, the flow statistics vary only slightly. As a matter of fact, the flow properties and statistics are similar to those predicted by earlier computational studies which did not account for the free-surface descent. Furthermore, the

evaporation model employed herein provided predictions for the evaporative mass flux that agree very well with available experimental data.

4.2 Comparative study of the four cases

In this section, we compare the results of our WMLES for the 4 cases comprising our study. As already mentioned, the bottom and initial free-surface temperatures are kept the same in all cases but the initial height H_0 hence Ra_0 are different from case to case. The values of the initial height and free-fall velocity have been given in Table 1 above.

The profiles of the evolution of the average free-surface temperature $\langle \widetilde{T}_{\rm int} \rangle_{xz}$ are provided in Figure 10 in dimensionless form. The main feature of $\langle \widetilde{T}_{\rm int} \rangle_{xz}$ is that it decreases slowly over time as a consequence of water loss and the drop of the Rayleigh number. As mentioned above, this implies that, as time advances, diffusive heat transfer is favored over convective one. Nonetheless, this decrease is not monotonic but subject to small-amplitude oscillations. Similar profiles were predicted in DNS that solved for the flow in the water and the air above but at lower Ra_0 (Carlier and Papalexandris, 2023, 2024).

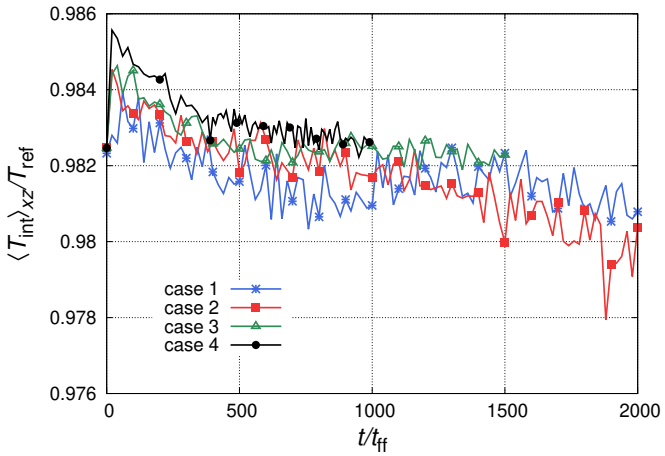


Fig. 10 Comparative study: evolution of the area-averaged temperature of the free surface for the 4 cases considered herein

Similarly, the profiles of the evaporative mass flux, shown in Figure 11a, are very close and display only small deviations from one another. This is to be expected since, for fixed ambient conditions above the free surface, $\langle \dot{m}'' \rangle_{xz}$ is mainly controlled by $\langle \widetilde{T}_{\rm int} \rangle_{xz}$. One can further observe that the difference between $\langle \dot{m}'' \rangle_{xz}$ in cases 1 and 2 has increased after $t = 1000\, t_{\rm ff}$. However, one would need to run the simulation for much longer times to establish whether such a difference persists or not. As an illustration, in Table 4 we provide the instantaneous values of $\langle \widetilde{T}_{\rm int} \rangle_{xz}$ and $\langle \dot{m}'' \rangle_{xz}$ at two different time instances, $t = 500$ and $1000\ t_{\rm ff}$. According to the values listed therein, at $t = 1000\, t_{\rm ff}$ the variation of $\langle \widetilde{T}_{\rm int} \rangle_{xz}$ from case to case is approximately 0.5 K , while the variation of $\langle \dot{m}'' \rangle_{xz}$ is less than 1.6%.

It is noted that the variation of the evaporative flux from case to case does not necessarily imply that this flux decreases as Ra rise. This is because in our study we modify the initial Rayleigh number by changing the initial height of the flow domain only. Whereas the bottom and initial free-surface temperatures are kept the same in all cases. As such, the evaporative flux is initially the same in all

cases. Consequently, there is no direct correlation between the changes of $\langle \dot{m}'' \rangle_{xz}$ from case to case and Ra_0.

The evolution of the water height is plotted in Figure 11b. Since $\langle \dot{m}'' \rangle_{xz}$ and $\langle \widetilde{T}_{\rm int} \rangle_{xz}$ vary slowly over time, then the drop of H is practically linear. In this figure, the slope of $\frac{H}{H_0}$ in the various cases becomes smaller as Ra_0 increases; this trend however is only due to the fact that the reference length H_0 varies from case to case. In absolute terms, the rate of descent does not change significantly because $H(t)$ is a function of $\langle \frac{\dot{m}''}{\widetilde{\rho}_{\rm int}} \rangle_{xz}$ only, which varies only slightly from case to case.

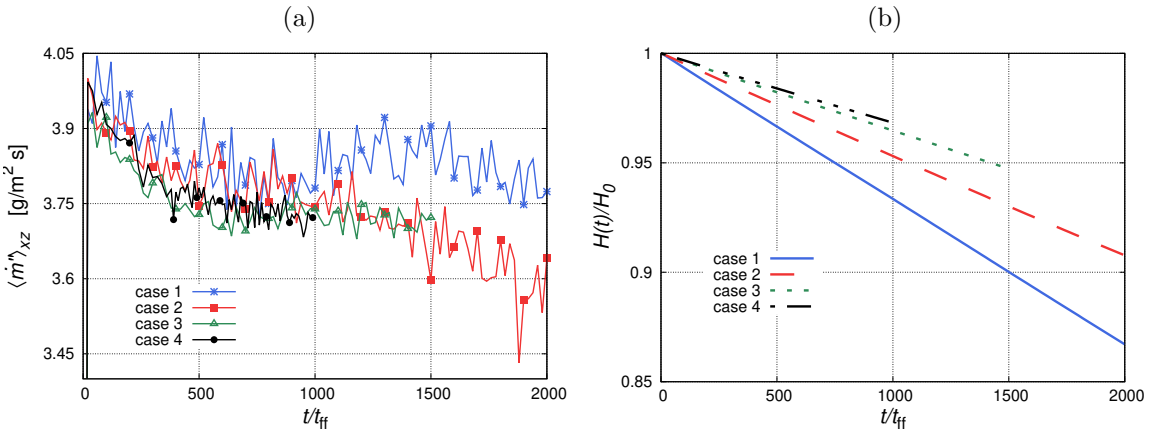


Fig. 11 Comparative study: (a) evolution of the evaporative mass flux $\langle \dot{m}'' \rangle_{xz}$; (b) evolution of the water height H

Table 4 Comparative study: area-averaged evaporative mass flux and free-surface temperature at two different time instances. It is noted that these are instantaneous results

	$t = 500\,t_{\rm ff}$		$t = 1000\,t_{\rm ff}$	
	$\langle \dot{m}'' \rangle_{xz}$ [g/(m^{2}s)]	$\langle \widetilde{T}_{\rm int} \rangle_{xz}$ [K]	$\langle \dot{m}'' \rangle_{xz}$ [g/(m^{2}s)]	$\langle \widetilde{T}_{\rm int} \rangle_{xz}$ [K]
case 1	3.83	352.68	3.78	352.46
case 2	3.75	352.77	3.74	352.72
case 3	3.73	352.99	3.74	353.02
case 4	3.78	353.31	3.72	353.04

We proceed to compare the flow statistics of the four cases considered herein. As mentioned above, for all cases, time-averaging period is performed between $t = 300\,t_{\rm ff}$ and the end of the simulation. For cases 1 and 2, the simulation ran until $t = 2000\,t_{\rm ff}$. However, for purposes of computational savings, for case 3 it ran until $t = 1500\,t_{\rm ff}$ and for case 4 until $t = 1000\,t_{\rm ff}$. Nonetheless, on the basis of our findings for case 2, the averaging periods for cases 3 and 4 are deemed sufficient for the reliable computation of flow statistics.

In Figure 12, we present the profiles of the mean normalized temperature $\langle \Theta \rangle$. As expected, the profiles becomes steeper in the bulk and they shift further to the left, *i.e.* towards the upper part of the domain, as the Rayleigh number increases. These properties are direct consequence of the fact that turbulence intensity enhances mixing and convective heat transfer. In the upper part of the domain, convective heat transport becomes more pronounced than in the lower part because of the

absence of hydrodynamic boundary layer at the free surface. This, in turn, causes the asymmetry of the profile of $\langle\Theta\rangle$ and its shift to the left.

In the same figure it is also interesting to observe that the thermal boundary layers become thinner as Ra_0 increases. Further, due to enhanced turbulent mixing in the upper part of the flow domain, the top thermal boundary layer is thinner than the bottom one. The difference between the thicknesses of the bottom and top layers also increases as Ra_0 becomes higher.

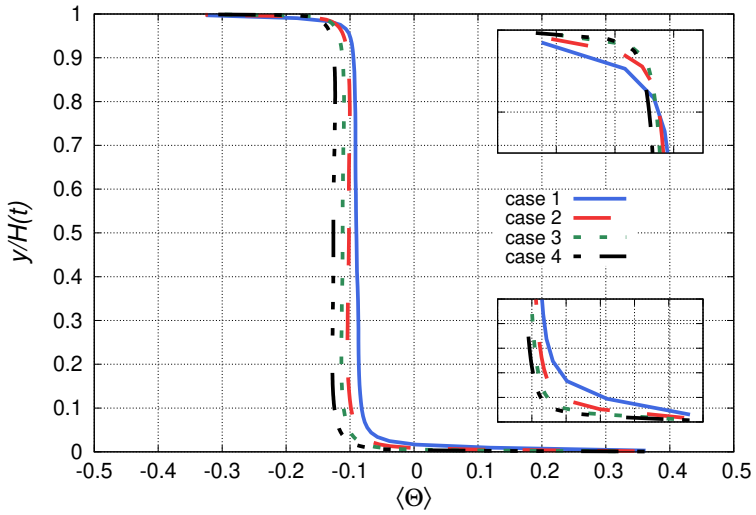


Fig. 12 Comparative study: profiles of the normalized temperature $\langle\Theta\rangle$. The inserts provide details of the profiles in the edges of the thermal boundary layers

In Figure 13 we provide the plots of the rms of the normal and in-plane velocity fluctuations. The profiles are similar and have the same features as those discussed in the previous section. Further, from these plots we infer that the dimensionless rms values (with respect to the free-fall velocity) do not change appreciably with Ra_0 . The most important difference between the various cases is a small decrease of the peak of $v_{\rm rms}$ $\bar{u}_{\rm rms}$ in the bulk as Ra_0 increases. Similarly, the peak of $\bar{u}_{\rm rms}$ near the bottom falls slightly with Ra_0. The location of this peak also marks the edge of the hydrodynamic boundary layer. As Ra_0 rises, this peaks moves closer to the wall, *i.e.* the boundary layer becomes thinner, as expected.

With regard to the boundary layers, it is noted that even though the cases considered herein are in the hard-turbulence range, they still fall in the so-called classical convection regime. In this regime, the boundary layers adjacent to solid walls are laminar or transitionary. Indeed, for water, the transition to the ultimate regime, in which the boundary layers are fully turbulent (Lohse and Shishkina, 2024), occurs around $Ra = 10^{12}$.

At this point a comment on the effect of non-Oberbeck-Boussinesq conditions is appropriate. In the present study we did not perform any simulations under the Oberbeck-Boussinesq approximation. Nonetheless, according to earlier numerical studies of our group (Hay and Papalexandris, 2019), the shift of the profile of $\langle\Theta\rangle$ to the left is mainly due to the top boundary condition. In other words, with water as the working medium, non-Oberbeck-Boussinesq conditions cause only a small modification to the profile of $\langle\Theta\rangle$. The effect of these conditions is more discernible in the second-order flow statistics. Evidently, the magnitude of this effect depends on the sensitivity of the fluid properties to the temperature and on the top-bottom temperature difference.

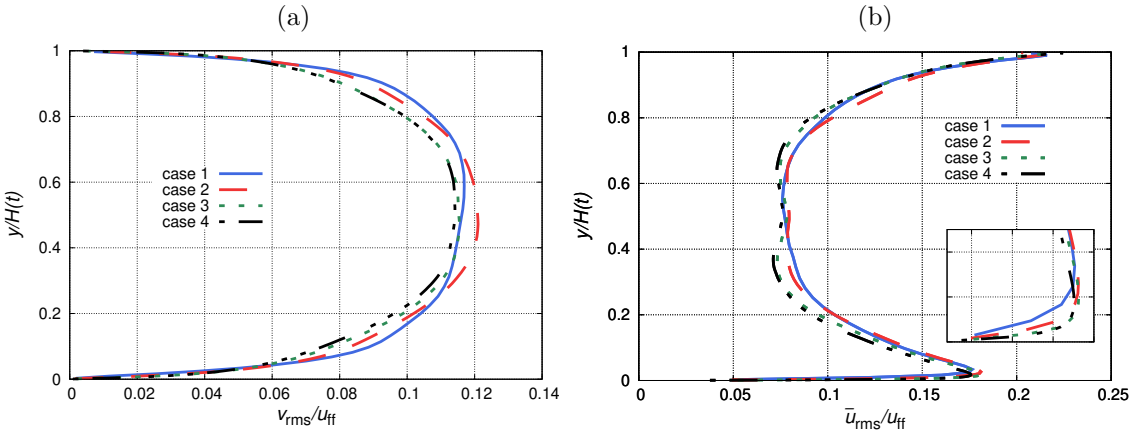


Fig. 13 Comparative study: profiles of the rms of the velocity fluctuations. (a) vertical velocity, v_{rms}; (b) in-plane velocity, $\bar{u}_{\mathrm{rms}}$. The insert show details of the $\bar{u}_{\mathrm{rms}}$ profile near the bottom wall

Profiles of the convective component of the Nusselt number for the 4 cases considered herein are shown in Figure 14. Since Ra decreases during the simulation due to water evaporation, so does the Nusselt number. Further, these plots confirm that the Nu_{conv} hence Nu increase significantly with Ra. With regard to the scaling of Nu with Ra, it can be readily confirm that the Nusselt number does not follow classical correlations for natural convection in a box such as the one of Niemala et al. (2000). This is due to enhanced convection near the free surface which translates to higher Nu. Moreover, at high Ra, our numerical results for Nu deviate from those of correlation (29). This is not surprising since that correlation was derived from simulations of convection at lower Ra and, therefore, it is not expected to be accurate for the cases examined in this study.

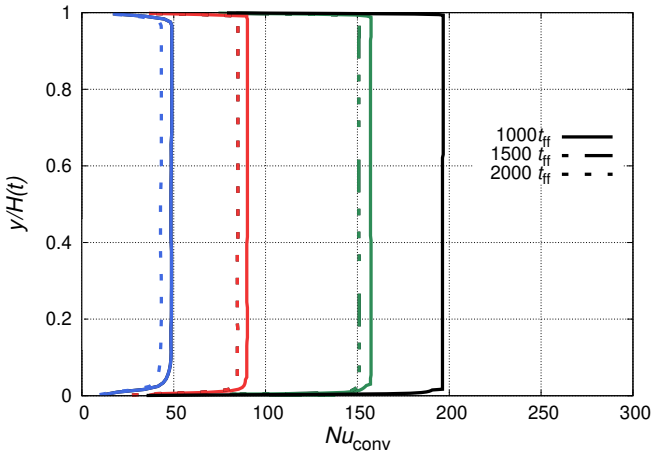


Fig. 14 Comparative study: profiles of the convective Nusselt number Nu_{conv} at different time instances. The profiles for cases 1, 2, 3 and 4 are shown from left to right (in blue, red, green and black color, respectively)

Accordingly, we propose herein the following $Nu - Ra$ scaling which is derived by fitting the results of our simulations,

$$Nu \;=\; 0.138\, Ra^{0.316}\,. \tag{36}$$

It turns out that this scaling approximates accurately the numerical result of Hay and Papalexandris (2020) in the range $7.5 \times 10^6 < Ra < 1.3 \times 10^8$ as well. It therefore covers a wider range of Ra and, in particular, most of the classical convection regime.

In Figure 15 we provide plots of the proposed $Nu - Ra$ scaling (36) and correlation (29). In the same figure we have also included the predictions of our WMLES for the Nusselt number. From this figure we can readily verify that (29) provides accurate predictions at low Ra but underestimates Nu at higher Ra. Moreover, the deviation between numerical results and (29) increases as Ra does. On the other hand, the proposed scaling remains accurate in the entire range of Ra.

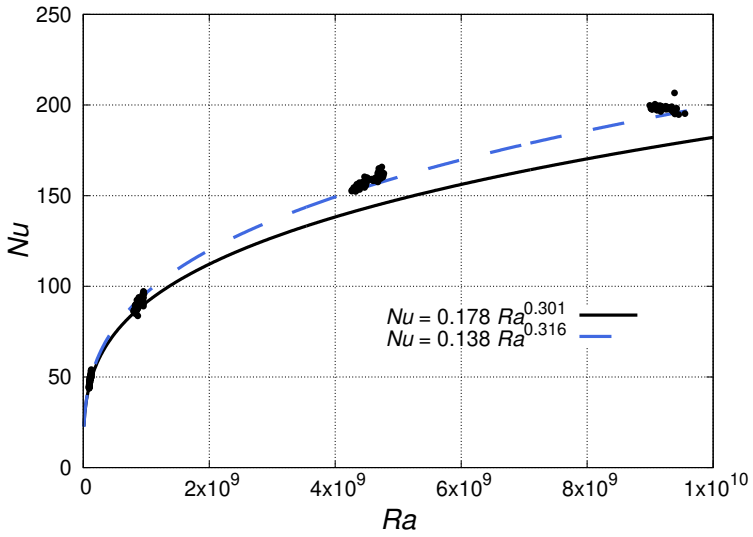


Fig. 15 Ra–Nu scaling. The black dots correspond to the numerical predictions of our WMLES for different time-averaging periods, *i.e.* for different final Rayleigh number. The dotted line (in blue) corresponds to the proposed scaling (36), while the solid line corresponds to (29)

As an illustration, in Table 5 we have listed our numerical results for Nu and Ra, for the 4 cases studied herein and at two different time instances, namely, $t = 1000$ and $t = 1500\, t_{\rm ff}$, respectively. In this table we also provide the predictions from correlation (29) and from the proposed scaling (36). From the values listed therein, we can verify that the deviation of (29) from our predictions is more than 10% for Ra greater than 10^9. On the other hand, (36) remains accurate as Ra increases.

Table 5 Comparative study: Rayleigh number, Nusselt number from WMLES and from correlations (29) and (36) at $t = 1000$ and $1500\, t_{\rm ff}$

	$t = 1000\, t_{\rm ff}$				$t = 1500\, t_{\rm ff}$			
	Ra	Nu	Corr. (29)	Corr. (36)	Ra	Nu	Corr. (29)	Corr. (36)
case 1	1.14×10^8	49.35	47.42	48.56	9.86×10^7	47.12	45.35	46.34
case 2	8.91×10^8	91.47	87.98	92.92	8.68×10^8	87.64	87.28	92.14
case 3	4.47×10^9	158.82	142.98	154.7	4.26×10^9	152.53	140.92	152.36
case 4	9.03×10^9	197.6	176.64	193.14				

Finally, we may add that the exponent of the proposed scaling (36) is close to the power-law fit of Niemala et al. (2000), $Nu = 0.124 Ra^{0.309}$. However, as mentioned above, the values of Nu obtained via this fit are substantially lower than those from (36), due to the free-slip condition at the top boundary which enhances convection.

5 Conclusions

In this article we presented a numerical study of natural convection in a water pool with evaporation across the free surface. Our study was based on the WMLES approach according which the boundary-layer structure is not resolved but suitably modeled, which provides significant computational savings. Evaporation across the free surface is estimated via a dynamic and inhomogeneous evaporation model. The loss of water due to evaporation and the descent of the free surface are accounted for by regularly reducing the height of the flow domain and applying a remeshing procedure.

Numerical results were provided for 4 cases at different Rayleigh numbers, ranging from $Ra = 1.35\times10^8$ to $Ra = 10^{10}$. According to our simulations, the free-surface temperature and evaporation rate decrease slowly over time. This may be attributed to the descent of the free surface which causes a slow, gradual decrease of the turbulence intensity. The numerical results for the evaporative mass flux are in very good agreement with available experimental data. Our simulations predicted that the flow is organized in a single-roll large scale circulation aligned in a diagonal plane with smaller convective rolls near the corners of the domain. Further, the profile of the mean normalized temperature is shifted to the left (toward the upper part of the domain). This asymmetry is attributed to the absence of a hydrodynamic boundary layer at the free surface, which enhances thermal mixing and convective heat transfer in its vicinity. On the other hand, the evaporation and the spatial variations of the free-surface temperature have only a minor effect on the structure of the convective patterns and the dynamics of the flow turbulence.

Our simulations showed that the Nusselt number increases substantially with the Rayleigh number and does not follow well-known $Nu - Ra$ correlations for natural convection in the box. Also, on the basis of the numerical results obtained in this study, we proposed herein a new $Nu - Ra$ scaling for natural convection in pools and cavities that covers a large range of turbulence intensities in the classical convection regime.

Acknowledgements. The authors gratefully acknowledge the financial support provided by the Belgian Federal Public Service Economy.

Declarations

- Funding: This research was funded by the Belgian Federal Public Service Economy under the Energy Transition Fund, project SFP-LOCA.
- Conflict of interest/Competing interests: The authors declare that they have no conflict of interest.
- Data availability: All data are available upon request.

References

Ahlers, G., Grossmann, S., Lohse, D.: Heat transfer and large scale dynamics in turbulent Rayleigh-Bénard convection. Rev. Mod. Phys. **81**(2), 503–537 (2009)

Balay, S., et al.: PETSc Web page (2025). https://petsc.org

Bodenschatz, E., Pesch, W., Ahlers, G.: Recent developments in Rayleigh-Bénard convection. Annu. Rev. Fluid Mech. **32**(1), 709–778 (2000)

Bower, S.M., Saylor, J.R.: A study of the Sherwood–Rayleigh relation for water undergoing natural convection-driven evaporation. Int. J. Heat Mass Tran. **52**, 3055–3063 (2009)

Bower, S.M., Saylor, J.R.: A study of the Sherwood-Rayleigh relation for water undergoing natural convection-driven evaporation. Int. J. Heat Mass Tran. **52**, 3055–3063 (2009)

Cabot, W., Moin, P.: Approximate wall boundary conditions in the Large-Eddy-Simulation of high Reynolds number flow. Flow Turbul. Combust. **63**, 269–291 (2000)

Carlier, J., Papalexandris, M.V.: An efficient tracking method of evaporative and flat free surfaces for turbulent convection. Comput. Fluids **257**, 105882 (2023)

Carlier, J., Papalexandris, M.V.: Turbulent natural convection in an air–water system with evaporation across the free surface. Int. J. of Multiphas. Flow **177**, 104873 (2024)

Ceresiat, L., Papalexandris, M.V.: Assessment of thermal boundary models for large eddy simulations of natural convection. Flow Turb. Combust. **114**, 117–144 (2025)

Carlier, J., Podvin, B., Papalexandris, M.V.: Turbulent natural convection in an air–water system with evaporation across the free surface. under review (2025)

Chillà, F., Schumacher, J.: New perspectives in turbulent Rayleigh-Bénard convection. Eur. Phys. J. E **35**(7), 58 (2012)

Deacon, E.L.: Gas transfer to and across an air-water interface. Tellus **29:4**, 363–374 (1977)

Demou, A.D., Scapin, N., Crialesi-Esposito, M., Costa, P., Spiga, F., Brandt, L.: Effects of Rayleigh and Weber numbers on two-layer turbulent Rayleigh-Bénard convection. J. Fl. Mech. **996**, 23 (2024)

Eidson, T.M.: Numerical simulation of the turbulent Rayleigh-Bénard problem using subgrid modelling. J. Fluid Mech. **158**, 245–268 (1985)

Grossmann, S., Lohse, D.: Scaling in thermal convection: a unifying theory. J. Fluid Mech. **407**, 27–56 (2000)

Grossmann, S., Lohse, D.: Thermal convection for large Prandtl numbers. Phys. Rev. Lett. **86**(15), 3316–3319 (2001)

Grossmann, S., Lohse, D.: Multiple scaling in the ultimate regime of thermal convection. Phys. Fluids **23**(4), 045108 (2011)

Hay, W.A., Martin, J., Migot, B., Papalexandris, M.V.: Turbulent thermal convection driven by free-surface evaporation in cuboidal domains of different aspect ratios. Phys. Fluids **33**(1), 015104 (2021)

Hay, W.A., Papalexandris, M.V.: Numerical simulations of turbulent thermal convection with a free-slip upper boundary. P. Roy. Soc. A-Math. Phy. **475**, 20190601 (2019)

Hay, W.A., Papalexandris, M.V.: Evaporation-driven turbulent convection in water pools. J. Fluid Mech. **904**, 14 (2020)

Jodat, A., Moghiman, M., Anbarsooz, M.: Experimental comparison of the ability of Dalton based and similarity theory correlations to predict water evaporation rate in different convection regimes. Heat Mass Tran. **48**, 1937–1406 (2012)

Kumar, N., Arakeri, J.H.: Natural convection driven evaporation from a water surface. Procedia IUTAM **15**, 108–115 (2015). IUTAM Symposium on Multiphase Flows with Phase Change: Challenges and Opportunities

Kays, W.M.: Turbulent Prandtl number. Where are we? ASME J. Heat Trans. **116**(2), 284–295 (1994)

Kays, W.M., Crawford, M.E.: Convective Heat and Mass Transfer, 3rd edn. McGraw-Hill, New York (1993)

Kawai, S., Larsson, J.: Wall-modeling in Large-Eddy-Simulation: Length scales, grid resolution, and accuracy. Phys. Fluids **24**(1), 015105 (2012)

Liu, H.-R., Chong, K.L., Ng, C.S., Verzicco, R., Lohse, D.: Enhancing heat transport in multiphase Rayleigh-Bénard turbulence by changing the plateliquid contact angles. J. Fl. Mech. **933**, 1 (2022)

Liu, H.-R., Chong, K.L., Wang, Q., Ng, C.S., Verzicco, R., Lohse, D.: Two-layer thermally driven turbulence: mechanisms for interface breakup. J. Fluid Mech. **913**, 9 (2021)

Liu, H.-R., Chong, K.L., Yang, R., Verzicco, R., Lohse, D.: Heat transfer in turbulent Rayleigh-Bénard convection through two immiscible fluid layers. J. Fl. Mech. **938**, 31 (2022)

Lemmon, E.W., Huber, M.L., McLinden, M.O.: NIST Standard Reference Database 23: Reference Fluid Thermodynamic and Transport Properties - REFPROP, 9.0 edn. Gaithersburg (2010)

Larsson, J., Kawai, S., Bodart, J., Bermejo-Moreno, I.: Large-Eddy-Simulation with modeled wall-stress: recent progress and future directions. Mech. Eng. Rev. **3**(1), 15–00418 (2016)

Lienhard, J.H. IV, Lienhard, J.H. V: A Heat Transfer Textbook. Dover, Mineola, NY (2019)

Lloyd, J.R., Moran, W.R.: Natural convection adjacent to horizontal surface of various planforms. J. Heat Transfer **96**(4), 443–447 (1974)

Lessani, B., Papalexandris, M.V.: Time-accurate calculation of variable density flows with strong temperature gradients and combustion. J. Comput. Phys. **212**(1), 218–246 (2006)

Lessani, B., Papalexandris, M.V.: Numerical study of turbulent channel flow with strong temperature gradients. Int. J. Numer. Method. H **18**, 545–556 (2008)

Lohse, D., Shishkina, O.: Ultimate Rayleigh-Bénard turbulence. Reviews of Modern Physics **96**(3), 035001 (2024)

Lohse, D., Xia, K.-Q.: Small-scale properties of turbulent Rayleigh-Bénard convection. Ann. Rev. Fluid Mech. **42**, 335–364 (2010)

Marrero, T.R., Mason, E.A.: Gaseous diffusion coefficients. Journal of Physical and Chemical Reference Data **1**(1), 3–118 (1972)

Martin, J., Migot, B.: Experimental study of the surface evaporation rate of a heated water pool at high temperature using infrared thermography. In: 18th International Topical Meeting on Nuclear Reactor Thermal Hydraulics, pp. 2302–2313 (2019). American Nuclear Society Portland, Oregon

Marichal, J., Papalexandris, M.V.: On the dynamics of the large scale circulation in turbulent convection with a free-slip upper boundary. Int. J. Heat Mass Tran. **183**, 122220 (2022)

Marshall, J., Schott, F.: Open-ocean convection: observations, theory, and models. Rev. Geophys. **37**(1), 1–64 (1999)

Nicoud, F., Ducros, F.: Subgrid-scale stress modelling based on the square of the velocity gradient tensor. Flow Turbul. Combust. **62**, 183–200 (1999)

Niemala, J.J., Skrbek, L., Sreenivasan, K.R., Donnelly, R.J.: Turbulent convection at very high Rayleigh numbers. Nature **404**, 837–840 (2000)

Paolucci, S.: Filtering of sound from the Navier–Stokes equations. NASA STI/Recon Technical Report N **83**, 26036 (1982)

Papalexandris, M.V.: On the applicability of Stokes hypothesis to low-Mach-number flows. Continuum Mech. Therm. **32**(4), 1245–1249 (2020)

Peng, S.-H., Hanjalic, K., Davidson, L.: Large-Eddy-Simulation and deduced scaling analysis of Rayleigh-Bénard convection up to $Ra = 10^9$. J. Turbul. **7**, 66 (2006)

Poling, B.E., Prausnitz, J.M., O'Connell, J.P.: The Properties of Gases and Liquids. McGraw Hill, New York (2001)

Poós, T., Varju, E.: Review for prediction of evaporation rate at natural convection. Heat Mass Transfer **55**, 1651–1660 (2019)

Quinn Brewster, M.: Evaporation of water at high mass-transfer rates by natural convection air flow with application to spent-fuel pools. Int. J. Heat Mass Tran. **116**, 703–714 (2018)

Reichardt, H.: The principles of turbulent heat transfer, Transl. by PA Scheck in Recent Advances in Heat and Mass Transfer, ed. by JP Hartnett. McGraw-Hill (1961)

Sagaut, P.: Large Eddy Simulation for Incompressible Flows, 3rd edn. Springer, Berlin (2006)

Scapin, N., Demou, A.D., Brandt, L.: Evaporating Rayleigh–Bénard convection: prediction of interface temperature and global heat transfer modulation. J. Fluid Mech. **957**, 12 (2023)

Shishkina, O., Stevens, R.J., Grossmann, S., Lohse, D.: Boundary layer structure in turbulent thermal convection and its consequences for the required numerical resolution. New J. Phys. **12**(7), 075022 (2010)

Shishkina, O., Thess, A.: Mean temperature profiles in turbulent Rayleigh-Bénard convection of water. J. Fluid Mech. **633**, 449–460 (2009)

Stevens, R.J.A.M., Verzicco, R., Lohse, D.: Radial boundary layer structure and Nusselt number in Rayleigh-Bénard convection. J. Fluid Mech. **643**, 495–507 (2010)

Viswanath, D.S., Kuloor, N.R.: On a generalized Watson's relation for latent heat of vaporisation. Can. J. Chem. Eng. **45**(1), 29–31 (1967)

Wang, Q., Liu, H.-R., Verzicco, R., Shishkina, O., Lohse, D.: Regime transitions in thermally driven high-Rayleigh number vertical convection. J. Fluid Mech. **917**, 6 (2021)

Zhang, L., Chong, K.L., Xia, K.-Q.: Moisture transfer by turbulent natural convection. J. Fluid Mech. **874**, 1041–1056 (2019)

Zikanov, O., Slinn, D.N., Dhanak, M.R.: Turbulent convection driven by surface cooling in shallow water. J. Fluid Mech. **464**, 81–111 (2002)